Biomaterials 31 (2010) 2955–2963

Contents lists available at ScienceDirect

Biomaterials

journal homepage: www.elsevier.com/locate/biomaterials

Quantification of the binding affinity of a specific hydroxyapatite binding peptide

Michael C. Weiger [a], Jung Jin Park [a,1], Marc D. Roy [a,2], Christopher M. Stafford [a], Alamgir Karim [b], Matthew L. Becker [a,c,*]

[a] Polymers Division, National Institute of Standards and Technology, Gaithersburg, MD 20899, USA
[b] Department of Polymer Engineering, University of Akron, Akron, OH 44325, USA
[c] Department of Polymer Science, University of Akron, Akron, OH 44325, USA

ARTICLE INFO

Article history:
Received 8 December 2009
Accepted 4 January 2010
Available online 27 January 2010

Keywords:
Surface plasmon resonance
Bioimaging
Hydroxyapatite
Phage display
Microfluidics
Peptides

ABSTRACT

The genesis of bone and teeth involves highly coordinated processes, which involve multiple cell types and proteins that direct the nucleation and crystallization of inorganic hydroxyapatite (HA). Recent studies have shown that peptides mediate the nucleation process, control HA microstructure or even inhibit HA mineralization. Using phage display technology, a short peptide was identified that binds to crystalline HA and to HA-containing domains of human teeth with chemical and morphological specificity. However, the binding affinity and specific amino acids that significantly contribute to this interaction require further investigation. In this study, we employ a microfluidic chip based surface plasmon resonance imaging (SPRi) technique to quantitatively measure peptide affinity by fabricating a novel 4 layer HA SPR sensor. We find the peptide (SVSVGMKPSPRPGGGK) binds with relatively high affinity ($K_D = 14.1 \mu M \pm 3.8 \mu M$) to HA. The independently measured amino acid fragment SVSV seems to impart a significant contribution to this interaction while the MKPSP fragment may provide a conformational dependent component that enhances the peptides affinity but by itself shows little specificity in the current context. These data show that together, the two moieties promote a stronger synergistic binding interaction to HA than the simple combination of the individual components.

1. Introduction

Normal and pathological mineralization of calcium phosphates are critical biological processes impacting both the medical and tissue engineering fields. One prominent polymorph of calcium phosphate essential during the normal mineralization processes of both teeth and bone matrix formation is hydroxyapatite (HA). Similarly, however, pathological derivatives of this mineral, such as carbonate-substituted hydroxyapatite, are implicated in osteoarthritis as well as other forms of degenerative arthritis [1]. As with all biological processes, a sensitive balance exists at multiple levels of regulation in which introduction or absence of one or more mediators can tip the balance in favor of normal or pathological biomineralization. The formation of the hydroxyapatite phase during normal biomineralization processes, such as osteogenesis and odontogenesis, is regulated by a complex orchestration of multiple cell types and numerous proteins. In the context of bone formation (osteogenesis), proteins such as bone sialoprotein, osteonectin, osteocalcin, and collagen I interact with HA to template the localized mineralization of HA, giving rise to the microstructures observed in bone which strongly contribute to its mechanical properties [2–6]. Similarly in tooth formation (odontogenesis), dentin matrix protein and statherin are implicated in regulating mineralization of calcium phosphate precursors into HA [7–9].

Despite the wealth of literature devoted to studying the bone biomineralization process during osteogenesis and identifying potential mediators, a coherent mechanism remains elusive due in part to the limitation of the current measurement methods. Indirect measurement techniques such as the von Kossa assay, ortho-cresolphthalein complexone, and Alizarin red [10–12] methods are destructive and purely endpoint measurements. Further, each method only identifies the presence of calcium and is not sensitive to the chemical composition or to the specific polymorphs of calcium phosphate such as HA [13]. Robust, new probes with both chemical and morphological specificity, perhaps coupled to a fluorescent

* Correspondence to: Matthew L. Becker, Department of Polymer Science, Goodyear Polymer Center, The University of Akron, Akron, OH 44325-3909, USA. Tel.: +1 330 972 2834; fax: +1 330 972 5290.
E-mail address: becker@uakron.edu (M.L. Becker).
[1] Present address: Department of Aerospace Engineering, University of Maryland, College Park, MD 20742, USA.
[2] Present address: Pfizer, New Haven, CT 06510, USA.

0142-9612/$ – see front matter © 2010 Elsevier Ltd. All rights reserved.
doi:10.1016/j.biomaterials.2010.01.012

reporter are necessary to advance our understanding of the HA mineralization process.

Small peptides are finding widespread utility as material specific probes. Several synthetic peptides containing amino acid sequences from HA interacting proteins, like those listed above, have been shown to promote or inhibit HA crystallization and interact directly with HA [2,8,9,14–16]. In efforts to improve upon nature, genetically engineered peptides that recognize other inorganic materials including Au, Ag, and Pt have been identified using combinatorial screening methods like phage display [17–22]. Recently, a peptide sequence that bound preferentially to HA over its amorphous calcium phosphate precursor was identified with phage display; however, measuring a quantitative binding affinity proved challenging [23]. Subsequent peptides that bind to calcium phosphate substrates have been found but again quantitative affinity measurements and insight into the mechanism of binding remain incomplete [24].

Investigators address these issues by using quartz crystal microbalance (QCM), atomic force microscopy (AFM) and surface plasmon resonance (SPR) [23,25–27]. SPR and SPR imaging have developed into major quantitative techniques for measuring the adsorption kinetics of small peptides onto a diverse set of material substrates [28,29]. However, a HA chip for use in the SPR imaging configuration was not previously available. In this effort, we used SPRi in conjunction with a novel HA coated sensor to quantify the binding affinity of a previously identified hydroxyapatite-binding peptide [23]. We further examine which amino acid segments contribute to the binding to aid future probe development while also lending insights into the potential mechanism(s) of binding.

2. Materials and methods

2.1. Peptides

Previously, phage display technology was used to identify the peptide sequence (HA-1, SVSVGMKPSPRPGGGK-biotin) which binds with high affinity to crystalline hydroxyapatite, as well as the hydroxyapatite-containing portions of human teeth [23]. This sequence, a scrambled sequence (Scram, PKGPSVMGGR-biotin) and two fragment sequences (HA-2, SVSVGGK-biotin; HA-3, VSMKPSPGGGK-biotin) were synthesized using standard *FMOC* solid phase peptide synthesis techniques with double coupling (Advanced ChemTech Apex 396), purified by dialysis in de-ionized water (molecular mass (MW) cutoff 1000 g/mol, cellulose membrane, Spectra) then dried and stored at −20 °C. Each peptide sequence contained a C-terminal biotin (*-b*) group. The dried peptides were re-hydrated in a 25 mmol/L 4-(2-hydroxyethyl)-1-piperazineethanesulfonic acid (HEPES) buffer made with ultra-pure de-ionized water (Milli-Q, Millipore).

2.2. Fabrication and characterization hydroxyapatite substrate

Hydroxyapatite (HA) substrates consisted of a base, glass substrate (25 mm × 50 mm, Fisher Scientific) which was cleaned by O_2 plasma treatment for 5 min (Plasma Prep Jr., SPI Supplies West Chester PA). To this base, thin films of Cr (0.6 nm), Ag (50 nm), TiO_2 (2.8 nm) and hydroxyapatite (10 nm–20 nm) were patterned by sequential layer sputtering in an argon atmosphere at 25 °C (Denton Vacuum Discovery-550). A custom target was used to create the thin layer of hydroxyapatite ($Ca_{10}(PO_4)_6(OH)_2$, Cerac Specialty Inorganics). The Cr and Ag layers were deposited using Direct Current (DC) mode, while TiO_2 and HA were deposited with Radio Frequency (RF) mode. The thicknesses of the individual layers were determined by both material deposition rates and Fresnel estimates. Surface morphology and uniformity were visualized by Atomic Force Microscopy (AFM, Veeco Dimension 3100) and Scanning Electron Microscopy (SEM, Zeiss Ultra-60). To prevent surface charging and enhance contrast during SEM imaging, samples were briefly sputtered with Au. The four films were also deposited on polished Si substrates (Wafer World, Inc) for SEM imaging and X-ray photoelectron spectroscopy (XPS) analysis. XPS was used to conduct an elemental analysis of the hydroxyapatite substrate. Spectra were obtained on a Kratos AXIS Ultra DLD spectrometer with a monochromatic Al x-ray source (1486.7 eV) operating at 140 W under 1.0×10^{-9} Torr vacuum. Measurements were performed in hybrid mode using electrostatic and magnetic lenses, and the take-off angle was 0° (angle between the sample surface normal and the electron optical axis of the spectrometer), which yields a maximum sampling depth of approximately 8 nm [30]. Atomic concentrations were calculated from survey spectra, collected over a binding-energy (BE) range from 1100 to 0 eV using a pass energy of 160 eV, energy resolution of 0.2 eV, and a 500 ms dwell time. High resolution (region) scans were collected using a pass energy of 20 eV and a sweep time of 60 s. The number of sweeps for survey and region scans was 2 and 3, respectively. A flood gun was used for charge neutralization, and all spectra were shifted with respect to the C 1s peak at 284.6 eV. Two spectra were acquired for each sample. A clean Si wafer specimen was also measured as a control. Peak areas for Ca 2s, P 2p, O 1s and C 1s were fitted using a Levenberg–Marquardt algorithm assuming a linear background (CasaXPS software).

2.3. Micro-channel construction

A multi-channel microfluidic device consisting of six, parallel flow channels measuring 40,000 μm × 300 μm × 120 μm (L × W × H) was constructed using standard soft lithographic techniques [31,32]. Briefly, Su8-50 photoresist (Micro Chem) was spun cast onto a Si wafer and then selectively polymerized using ultraviolet light shone through a lithographic mask containing the design, creating positive micro-channel features. Polydimethylsiloxane (PDMS, Dow Corning Sylgard 184) was then cast onto the patterned Si wafer, cured at 70 °C overnight, cut to size (50 mm × 25 mm) and then attached to the HA substrate to create an SPR compatible flow-cell.

2.4. Surface plasmon resonance (SPR) imaging setup

A custom SPR imaging system Kretschmann configuration, SPR BioSystems was built around a sapphire prism ($n = 1.77$) and 514 nm light emitting diode (LED) source (LE-1G, WT&T Inc). The reflected intensity (R) of both p- and s-polarized LED light (R_p and R_s) was collected with a cooled CCD camera (Retiga 2000RV, QImaging). Computer imaging software (StreamPix NorPix Inc.) was used to capture images of 1) reflected intensities from (R_p and R_s) illumination at different angles of incident and 2) images of reflected p-polarized light (R_p) at a fix incident angle as a function of time. ImageJ (Rasband, W.S., National Institute of Health, Bethesda, MD, USA, http://rsb.info.nih.gov/ij/) was used to extract from the collected images, the average intensities of a central region of interest (ROI, 600 pixels × 12 pixels) within an individual flow channel. Using capture method 1 and ImageJ, the characteristic reflectivity (R_p/R_s) vs. incident angle (θ) curve of each channel was constructed. This was done first for incident angles of 57°–85° at increments of 0.1°. Based on the position of the resonance angle (θ_R) incident θ at which the reflectivity (R_p/R_s) is a minimum), a second reflectivity (R_p/R_s) curve was constructed from a narrower range of incident angles (typically 66°–78° at 0.05°). The principally parabolic curve was fit to a 6th order polynomial using least square regression and the derivative of this function was calculated to identify the SPR imaging angle (θ_i), the angle that yields maximum sensitivity in R_p/R_s changes and corresponds to the inflection point of the R_p/R_s curve and is $< \theta_R$. For real time measurements of R_p using capture method 2, the incident angle was fixed at θ_i (typically 74°–76°). In this case, reflectivity (R_p/R_s) is calculated based on an initial measurement of R_s (θ_i) when determining the reflectivity curve and assumed to remain constant during the time course over which R_p is collected. This assumption appears to be valid because R_s did not change significantly over the duration of the experiment, presumably due to the stability of the LED illumination source.

2.5. Peptide binding experiments and SPR image analysis

All micro-channels were treated with a 5 mg/mL bovine serum albumin (BSA) solution for ≈ 1 h at 25 °C to minimize the non-specific adsorption of peptides to the PDMS during binding experiments. The PDMS micro-channels were then washed with de-ionized water (18 MΩ cm^{-1}) and dried. Finally, the channels were secured to the HA substrate and optically coupled to the prism of the SPR setup with immersion oil ($n = 1.522$). Peptide solutions were prepared in 25mM HEPES buffer (pH 7.4) at several concentrations (200, 100, 50, 25, and 10 μM). It should be noted that buffers containing sodium chloride (i.e., PBS or TBS buffers) could not be used with the HA substrate due to the ability of such buffers to penetrate the outer layers and react with the silver layer. Syringe pumps (Braintree Scientific Inc.) were used to introduce only HEPES buffer for 10 min–15 min at a flow rate of 2.5 μL/min to establish a baseline. After characteristic reflectivity curves were collected and the imaging angle set, a specific peptide concentration was flown into individual channels at a flow rate of 2.5 μL/min. Once an initial positive change in the average reflected intensity (p-polarized light) was observed, the peptide was infused for ≈ 45 s (≈1 channel volume) and then flow was stopped by turning the pump off and closing a syringe valve, creating a pseudo-static condition for steady-state measurements and allowing the system to approach equilibrium. Images of R_p were collected every 5 s for 20 min–30 min at 400 ms exposure time and converted to reflectivity (R_p/R_s) within the ROI. A baseline reflectivity $[R_p/R_s]_B$ value, time average of R_p/R_s values over the first 5 min, was subtracted from the R_p/R_s data set to yield the change in reflectivity ($\Delta(R_p/R_s)$), which is equivalent to the typical % R reported in the literature divided by 100%. This data treatment typically resulted in very small $\Delta(R_p/R_s)$ values that fluctuated around zero until peptide adsorption began (shortly after 5 min), indicated by increasing positive $\Delta(R_p/R_s)$ values. These positive $\Delta(R_p/R_s)$ values were reported and are theoretically proportional to the amount of peptide binding to the HA surface. From this data, peptide binding kinetics and steady-state behavior in

each channel were measured under the static conditions at 25 °C for 20 min–30 min or until the system approached equilibrium.

3. Results

3.1. Hydroxyapatite SPR chip fabrication

Combinatorial phage display has played an essential role in identifying specific peptide sequences that exhibit high affinity for both organic and inorganic materials. This technique was used previously to identify a novel peptide, consisting of 12 amino acids (Table 1, HA-1), that showed chemical and morphological specificity towards crystalline hydroxyapatite [23]. The binding constant and amino acid moieties contributing to the peptide affinity, however, were not quantitatively characterized. In order to complete the characterization of this peptide–mineral interaction, we employed surface plasmon resonance imaging (SPRi). This surface sensitive technique allows adsorption of small molecules to a substrate possessing a thin metal film (typically Au or Ag) to be monitored in real time by measuring changes in the intensity of reflected light, which corresponds to small changes in the refractive index at the surface. A custom built SPRi system was used to measure the peptide binding kinetics of the HA-1 peptide as well as two peptide fragments (HA-2 and HA-3) derived from HA-1. To account for any non-specific binding to a hydroxyapatite coated substrate, a scrambled peptide (Scram) was used. The amino acid sequences and general properties of the peptides used in this study are given in Table 1.

The ability to accurately measure any specific interaction between these small peptides and HA is dependent on the multilayer, sensor platform. We chose to build our SPRi sensor surface atop a basic glass (n = 1.522) substrate. Four thin films were sequentially sputtered on the glass substrate in a rectangular pattern (Fig. 1 a). The number, thickness and composition of each thin film affect the intensity and shape of the measured SPR signal, the reflectivity (R_p/R_s). Our sensor consisted of a very thin layer of Cr (0.44 nm–0.6 nm) to provide a robust adhesive layer for the second metal layer, Ag (50.7 nm–53.6 nm). Ag was chosen over Au because it provides the sharpest SPR signal, enhanced penetration length and is reported to have greater sensitivity to thickness and refractive index variations [33–37]. Despite these advantages, Ag is chemically unstable and prone to oxidation in both air and aqueous environments. To eliminate this disadvantage, a thin layer of TiO_2 (1.1 nm–2.8 nm) was deposited to both protect the Ag layer and provide an adhesive layer for the final HA (10 nm–20 nm) layer. To complete the SPR sensor, a microfluidic device with 6 parallel flow channels was fabricated using standard soft lithographic techniques [31,32] and attached to the SPR sensor (Fig. 1b). This flow-cell was optically coupled to the prism in our SPRi system with refractive index-matching immersion oil (Fig. 1 c and Materials and methods). When the prism is illuminated with p-polarized light at an incident angle (θ) above the critical angle, total internal reflection occurs. The evanescent wave that is generated excites surface plasmons, longitudinal charge density waves, which propagate along the interface between the Ag and adjacent layers. When the surface plasmons are maximally excited, a minimum in the R_p/R_s is observed and the incident angle at which this occurs is referred to as the resonance angle (θ_R). Both θ_R and the R_p/R_s (as a function of θ) are dependent on changes in the refractive index and thickness at the sensor surface. The peptides under investigation are flown into the flow-cell and their adsorption to the HA surface changes the local refractive index at the surface, which shifts the location of θ_R. Thus, the amount of peptide adsorbed to the surface is proportional to changes in θ_R as well as R_p/R_s under certain conditions. This $\Delta\theta_R$ is proportional to the density of adsorbed molecules at the surface [38]. In summary, the custom SPR imaging system designed and used here represents a hybrid SPR instrument that can make full angle resonance scans and single angle image scans for multiple parallel flow channels simultaneously. We use the angle resonance scans for characterization of the HA substrate and single angle imaging, reported here as $\Delta R_p/R_s$, for the kinetics of HA-1 peptide binding.

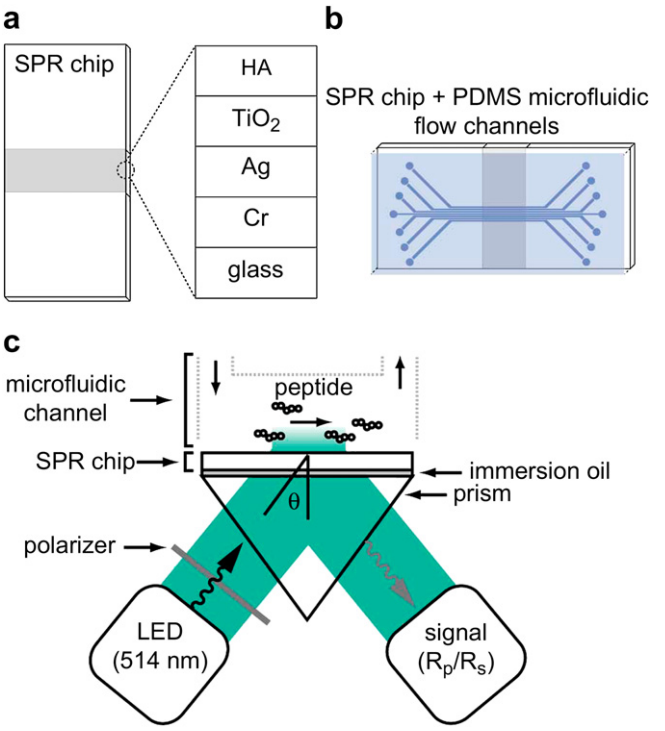

Fig. 1. Surface plasmon resonance imaging system. (a) A glass substrate (n = 1.522) was patterned by sputtering thin layers of Cr, Ag, TiO_2, and hydroxyapatite (HA) sequentially on a central region (≈10 × 25 mm). (b) This HA coated chip was then attached to a PDMS based microfluidic device containing six flow channels. (c) The coupled device is optically joined to a sapphire (n = 1.77) prism with immersion oil (n = 1.522). The image intensities of both reflected p- and s-polarized light from a 514 nm LED source is collected with a CCD camera. Peptides are introduced into a microfluidic channel and adsorption events are measured as changes in reflectivity, the ratio of reflected p- to s-polarized image intensities (R_p/R_s).

Table 1
Amino acid sequences and physicochemical properties of HA binding and non-binding peptides.

Peptide	Sequence	MW (g/mol)	Charge (e)[a]	Pi (pH unit)	GRAVY[b]
HA-1	SVSVGMKPSPRPGGGK-*b*	1767.3	3	11.82	−0.675
HA-2	SVSVGGK-*b*	934.2	1	9.69	0.213
HA-3	VSMKPSPGGGK-*b*	1288.7	2	10.8	−0.7
Scram	PKGPSVMGGR-*b*	1286.7	2	11.66	−0.718

NOTE: GGGK, GGK and GGR are glycine spacer sequences for biotin-*b*.
[a] e: elementary net charge.
[b] GRAVY: grand average hydropathicity.

3.2. SPR data modeling and interpretation

Every SPR sensor has a unique reflectivity curve with feature characteristics that are dependent on the thickness and refractive index of each layer. Due to the sensitivity of this technique to minute changes in the surface composition, it is essential that the

reflectivity curve describing the system be measured. First, we confirmed that our sensor supports surface plasmon generation by successfully measuring a reflectivity curve (Fig. 2 a). Next we used a multi-layer Fresnel model, implemented using a custom MATLAB code, to estimate the reflectivity (R_p/R_s) as a function of incident angle (θ) for our four layer sensor. After applying a least square parameter fit, the Fresnel description showed good agreement with our experimental data (Fig. 2 a) and gave thickness estimates for each layer [Cr (0.44 nm), Ag (53.6 nm), TiO_2 (1.1 nm) and HA (22 nm)] similar to those measured by deposition rate/sputter time [Cr (0.6 nm), Ag (50.7 nm), TiO2 (2.8 nm)], AFM and SEM [HA (10–25 nm)]. The change in reflectivity $\Delta(R_p/R_s)$ measured by our SPRi system, at a fixed θ, is proportional to $\Delta\theta_R$ (i.e. density of surface absorbed molecules); however, this relationship holds only for $\Delta(R_p/R_s) < 0.06$ (Fig. 2b). Further, our SPRi system is theoretically capable of detecting changes in refractive index of $\approx 5x10^{-5}$ refractive index units (RIU).

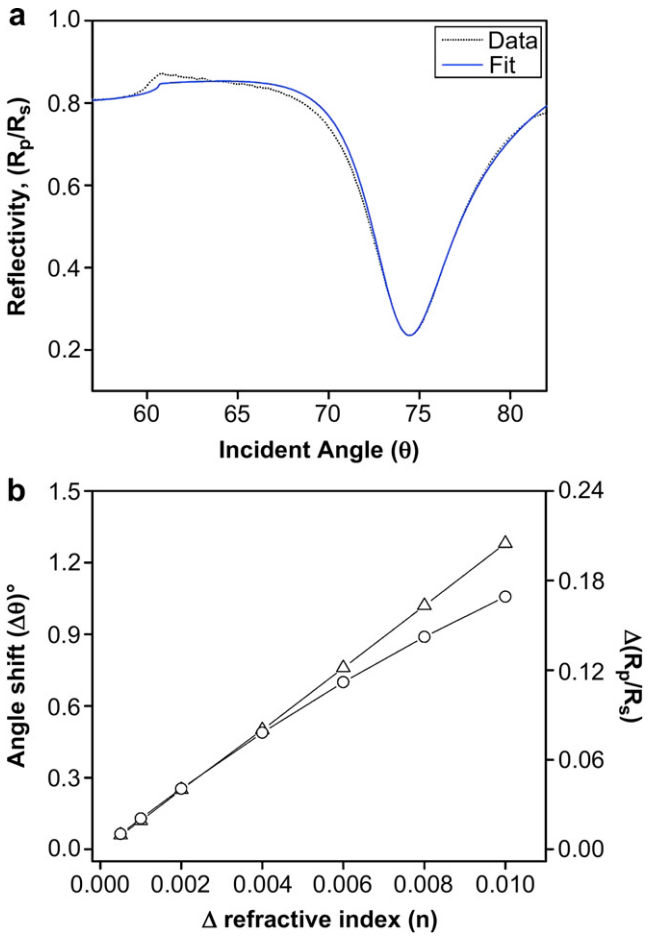

Fig. 2. Hydroxyapaite coated substrates support surface plasmon resonance and adsorption measurements. (a) Experimental reflectivity (R_p/R_s) ('data'-dashed line) measured as a function of the incident angle of LED light (514 nm) show the multi-layer chip exposed to water exhibits a classical surface plasmon resonance (SPR) curve with a clear resonance angle, incident angle at which R_p/R_s is minimum. The predicted curve of a six layer Fresnel model ('fit'-solid line) shows good agreement with experiential data and provides estimates for the thickness of each sputtered layer. (b) Changes in the refractive index (n) at the substrate surface, due to the adsorption of small molecules, will shift the SPR resonance angle (θ_R) to the right. A linear relationship exists between $\Delta\theta$ and Δn (triangles). SPR imaging relies on measuring changes in reflectivity $\Delta(R_p/R_s)$ at a fixed incident angle which is linearly proportional to Δn (circles) initially, but then deviates above 0.06 $\Delta(R_p/R_s)$ or 0.004 Δn. This implies that fixed angle, reflectivity measurements using the HA coated substrate and our SPRi system are only proportional to the density of adsorbed small molecules if $\Delta(R_p/R_s) < 0.06$.

3.3. Hydroxyapatite SPR chip characterization

Hydroxyapatite (HA) [$Ca_5(PO_4)_3(OH)$] is one of several forms of calcium phosphate (CP) including: amorphous calcium phosphate ACP [$Ca_3(PO_4)_2 \cdot xH_2O$], monocalcium phosphate [$Ca\cdot(H_2PO_4)$], dicalcium phosphates (DCPs) [$Ca(HPO_4)_2\cdot xH_2O$], tricalcium phosphates (TCPs)[α- and β- $Ca_3(PO_4)_2$], and octacalcium phosphate (OCP) [$Ca_8H_2(PO_4)_6\cdot xH_2O$]. Among these, HA is the most stable and is the prominent inorganic component in both teeth and bone. To generate thin films of HA for our SPRi sensor, a custom sputtering target was made by sintering crystalline HA (see Materials and methods). For characterization purposes, HA was sputtered onto a clean Si wafer and analyzed with x-ray diffraction (XRD) and x-ray photoelectron spectroscopy (XPS). Not surprisingly, XRD measurements yielded a very weak signal making reliable diffraction patterns difficult to discern from background (data not shown) [39]. With lattice constants $a = 0.9418$ nm and $c = 0.6884$ nm for HA, it is possible that the microscopic amounts and sizes of the sputtered HA crystallites in addition to their random orientations on the surface prevented detection of the classical XRD pattern,

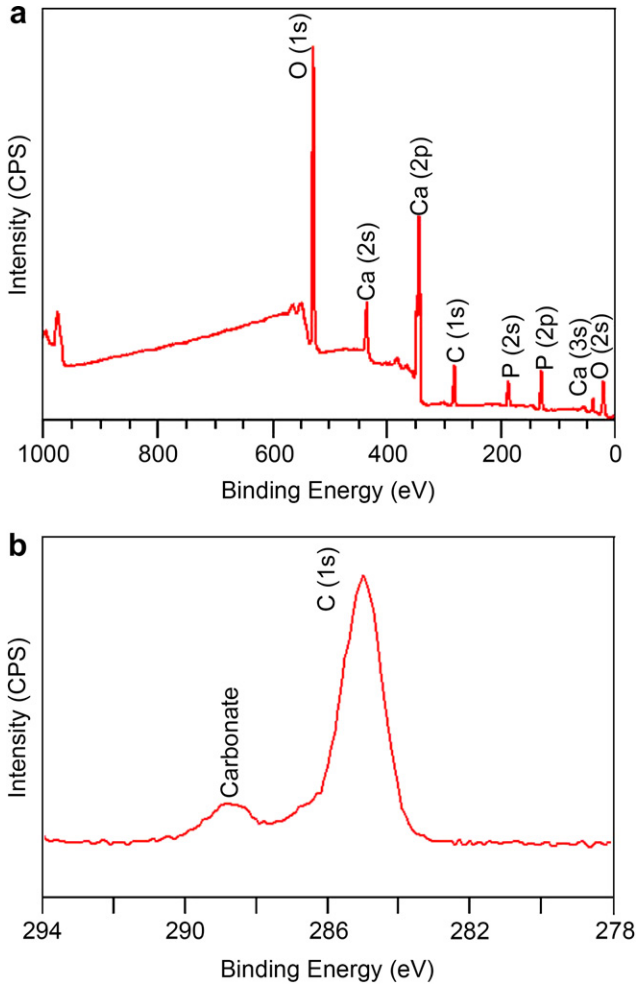

Fig. 3. XPS spectrum confirms the presence of hydroxyapatite. (a) A survey spectrum for a Si wafer sputtered with a thin layer of hydroxyapatite (10–20 nm) shows characteristic Ca, P, and O intensity peaks comparable to those found in the NIST standard reference material, but yields a higher Ca/P ratio (1.85) than the stoichiometric value for pure HA (1.667). (b) Inspection of carbon contamination, C (1s) XPS peak intensities, reveals a peak at higher binding engery (289.3 eV) which corresponds to carbonate (CO_3^{-2}). Taking into account that CO_3^{-2} ions can pair with Ca^{2+} and consider only Ca^{2+} and PO_4^{3+} pairings, an adjusted Ca/P ratio (1.52) was estimated which agrees with reported Ca/P values for HA determined using XPS (1.46–1.59).

typically seen for HA crystals 0.25 μm × 1.5 μm (width × length) [39–41]. Using XPS, we confirmed the presence of the elemental components of HA (Ca, P, and O) and found the survey spectrum qualitatively matched that reported in literature for the NIST standard reference HA (Fig. 3 a) [42]. Additionally, the peak positions of the Ca (2p), P (2p) and O (1s) orbitals correspond to the BEs reported in literature for HA [43](data not shown). In order to further confirm the phase(s) of calcium phosphate on the surface, we calculated the Ca/P from the XPS peak ratios of the core levels of the P (2p) and Ca (2p) orbitals. The stoichiometric Ca/P ratio for HA is 1.667; however, the XPS Ca/P ratios (Ca/P_{XPS}) reported for HA are consistently lower, ranging from 1.46 to 1.59 [42,44,45]. We initially calculated a relatively high $Ca/P_{XPS} = 1.85 \pm 0.03$ (mean ± standard deviation). Upon further examination of the survey spectrum, a small, secondary peak adjacent to the C (1s) peak was observed at 289 eV (Fig. 3b), which indicates the presence of carbonate (CO_3^{2+}) [42,43]. Carbonate can typically incorporate into various calcium phosphates, as $CaCO_3$, during synthesis due to the presence of CO_2 in the air and solutions [46,47]. An adjusted Ca/Pa_{XPS} ratio of 1.52 ± 0.06 was calculated according the method described by Lu et al. that takes into account the carbonate impurities. This value agrees well with those reported in literature and provides evidence that our surface is indeed coated with HA. Although we cannot rule out the possibility that a small fraction of β-TCP ($Ca/P_{XPS} \approx 1.40$) coexists with the HA, the presence of ACP ($Ca/P_{XPS} \approx 1.13$) and other unstable phases seems less likely [44]. The morphology of the sputtered HA was assessed by AFM and SEM (Fig. 4 a and b). Both methods showed a random, cobble-stone pattern with feature sizes on the order of <100 nm with a relative degree of microscopic heterogeneity and macroscopic uniformity similar to RF sputtered HA reported in literature [48–50].

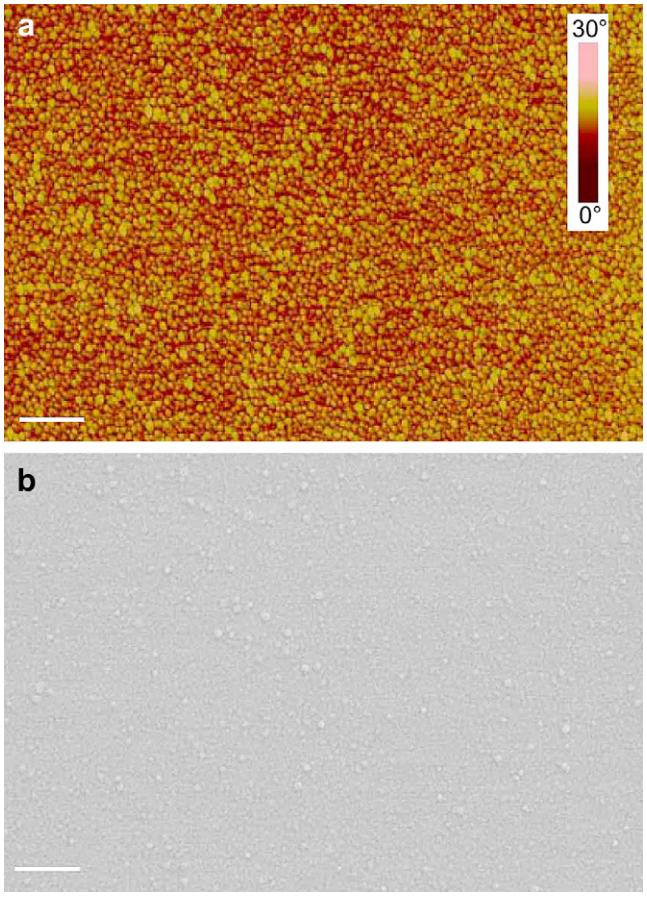

Fig. 4. RF sputtered HA shows random surface morphology and macroscopic uniformity. (a) AFM phase image (5 × 4 μm) acquired in dynamic force mode (DFM) shows nanometer sized islands randomly spaced across the surface of the multi-layer SPR sensor (Cr, Ag, TiO_2, and HA). Scale bar = 500 nm (b) SEM imaging of the SPR ship shows surface features analogous to those observed with AFM and reveals a level of microscopic heterogeneity. Scale bar = 500 nm.

3.4. HA-1 binding affinity

To characterize the binding affinity of our HA-1 peptide toward HA, we combined PDMS microfluidic channels and SPRi to deliver the peptide at a set concentration and then monitor the binding kinetics in real time. The experiments were conducted under quasi-static conditions (see methods) and the change in reflectivity $\Delta(R_p/R_s)$ was measured at various peptide concentrations. Fig. 5a shows average reflectivity measurements ($n = 3$) as a function of time for different concentrations of HA-1 peptide. For each HA-1 peptide concentration, the reflectivity approached an equilibrium

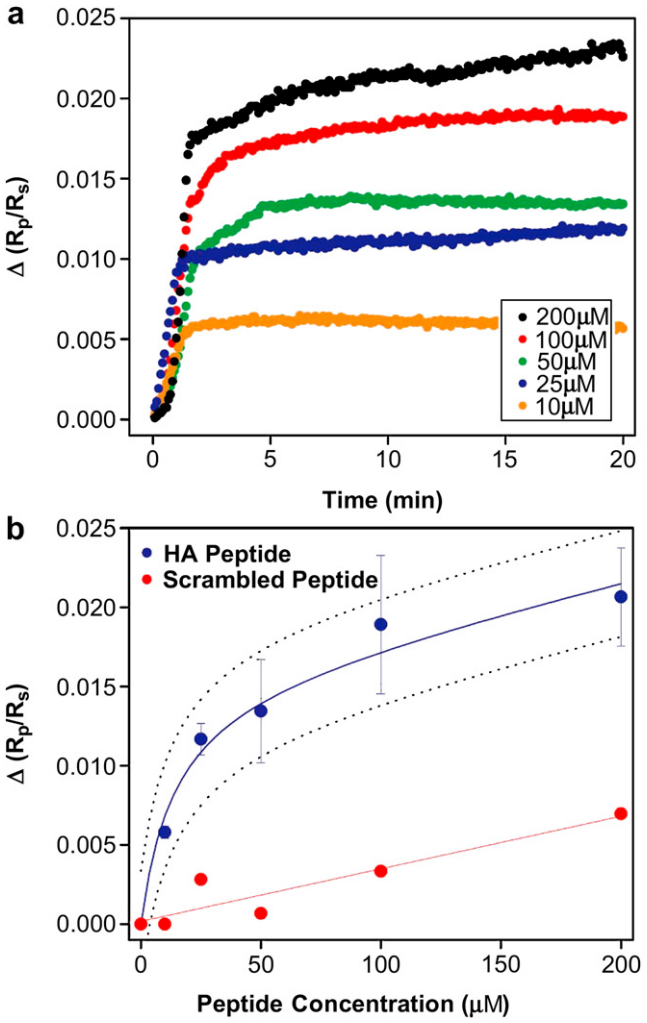

Fig. 5. HA-1 peptide binds with high affinity to hydroxyapatite coated substrate. (a) The adsorption kinetics as measured by the change in reflectivity $\Delta(R_p/R_s)$ vs. time of various HA-1 peptide concentrations (inset) were monitored using SPR imaging. Each kinetic profile approaches a concentration-dependent steady-state $\Delta(R_p/R_s)$. (b) Steady-state binding data for two peptides are shown; scrambled peptide (red symbols, $n = 1$) and the HA-1 peptide (blue symbols, $n = 3$). The scrambled peptide (Scram) bound non-specifically to the HA coated surface, while HA-1 exhibits both specific and non-specific binding characteristics. The solid lines and dashed lines represent model fits of the data and 95% confidence intervals, respectively. The error bars represent ± the standard error.

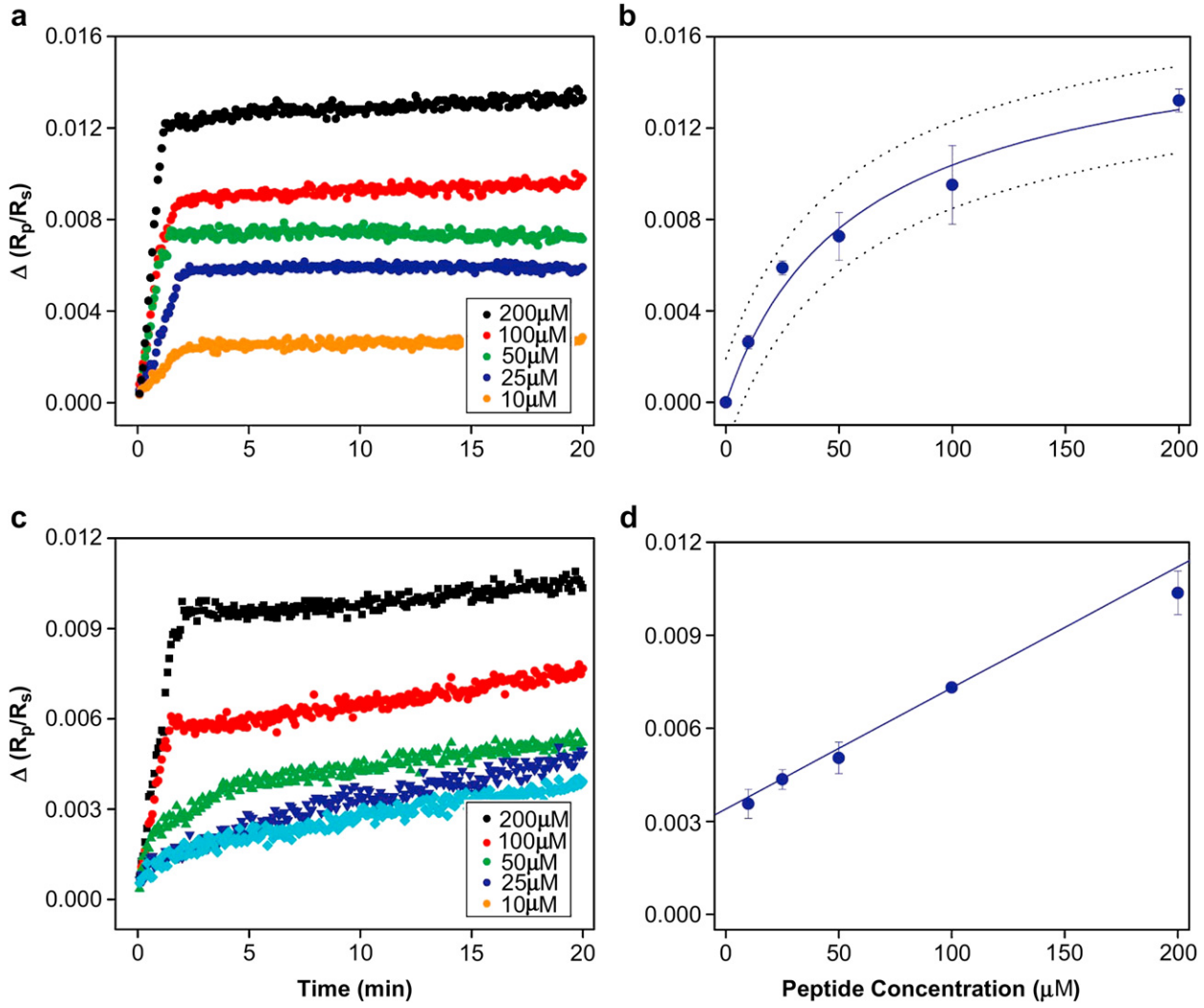

Fig. 6. HA-1 peptide fragments bind to hydroxyapatite. The adsorption kinetics, measured by the change in reflectivity $\Delta(R_p/R_s)$ vs. time, at various concentrations (inset) of the (a) HA-2 and (c) HA-3 peptide fragments were monitored using SPR imaging. Each profile shows concentration-dependent kinetics and steady-state $\Delta(R_p/R_s)$. Steady-state binding data for (b) HA-2 and (d) HA-3 (blue symbols, $n = 3$ for both) show specific and non-specific binding characteristics, respectively. The solid lines and dashed lines represent model fits of the data and 95% confidence intervals, respectively. The error bars represent ± the standard error.

after 20 min–30 min and stabilized at a value corresponding to amount of surface bound HA-1 peptide at equilibrium. The data also verify that our $\Delta(R_p/R_s)$ measurements fall within the range where $\Delta(R_p/R_s)$ is proportional to $\Delta\theta_R$ and thus, HA-1 peptide surface density. It was difficult to observe a clear concentration dependence in the rate of adsorption which we attribute to batch-to-batch variability in the HA substrates (Fig. 5a). Subsequent peptide binding experiments were carried out using HA substrates of the same batch and as expected a more clear concentration dependence was observed (Fig. 6). The measured equilibrium, $\Delta(R_p/R_s)$, however, still provided a robust measure of HA-1 peptide affinity to HA. The amount of HA-1 peptide bound at equilibrium appears to plateau as initial peptide concentration increases, suggesting saturation of HA binding sites with peptide and indicating specificity; but, the gradual, near linear increase at higher initial HA-1 peptide concentrations suggests non-specific binding, and possibly layering, was also occurring (Fig. 5b). To estimate the degree of non-specific binding, the HA substrate was challenged with a scramble peptide sequence (Scram). A linear relationship was observed between the Scram peptide $\Delta(R_p/R_s)$ bound at equilibrium versus initial Scram peptide concentration, indicating a low level of non-specific binding occurs on the HA substrate (Fig. 5b).

In order to quantify the affinity of both the specific and non-specific interactions, two simple models were applied to each data set. Model r^a describes both specific and non-specific peptide binding to the HA substrate (Table 2). This model assumes a monovalent, receptor (HA) and ligand (peptide) interaction, where the number of receptors/binding sites (HA crystals) remains constant and uniform, and that peptide depletion is negligible. Model r^b describes only the non-specific peptide binding and assumes that the rates of association and dissociation of the peptide are more rapid compared to the

Table 2
Fundamental model describing specific and non-specific interaction between the HA substrate and peptides.

Parameters	Description	Equations
r	reflectivity change, $\Delta R_p/R_s$	$r^a = \frac{B_{max}L_o}{(K_D + L_o)} + K_N L_o$
K_D	dissociation constant	
K_N	non-specific association constant	
B_{max}	maximum reflectivity change, $\Delta R_p/R_s$	$r^b = K_N L_o$
L_o	peptide concentration	

a = specific and non-specific binding model.
b = non-specific binding model.

respective association and dissociation rates for the specific peptide-HA interaction (Table 2). Lastly, all binding events, specific and non-specific, are assumed to be reversible. Fitting the equilibrium $\Delta(R_p/R_s)$ Scram peptide data to model r^b provided an estimate of the non-specific association constant K_N (Fig. 5b and Table 3). Additionally, B_{max} was estimated by calculating the difference of the average $\Delta(R_p/R_s)$ at 100 and 200 μM for the HA-1 peptide and Scram peptide signals, which can be thought of as an observed, maximum number of binding sites. This parameter was assumed to be constant and fixed for all subsequent fittings using model r^a. The K_N calculated from fitting the Scram peptide data provided the initial guess for the respective parameter in model r^a, which was used to fit the HA-1 peptide data and obtain a measure of the specific binding affinity, K_D. Both model fits effectively describe the data sets (Fig. 5b) and show excellent agreement in their estimate of K_N (Table 3). Further, we find that the HA-1 peptide binds with a $K_D = 14.1\,\mu M \pm 3.8\,\mu M$, a relatively high affinity considering the small size of the peptide and unique nature of HA.

3.5. HA-1 peptide fragment binding affinity

Next, we sought to augment our findings by investigating which amino acid segments in the HA-1 peptide, significantly impact the affinity to HA. To accomplish this, our HA substrate was challenged with two HA-1 peptide fragments: the HA-2 peptide, conserving the front portion of HA-1 and the HA-3 peptide, conserving the remaining tail portion. As described above, each peptide was delivered to our HA substrate at various initial concentrations, and the binding kinetics were monitored using SPRi (Fig. 6 a and c). There were apparent qualitative differences in the binding kinetics of these two peptides, both during the association phase and as equilibrium $\Delta(R_p/R_s)$ was approached. The adsorption kinetics of both peptides clearly exhibited a dependence on the initial peptide concentration (Fig. 6 a and c). Interestingly, we found very different modes of binding between these two peptides when the equilibrium $\Delta(R_p/R_s)$ as a function of the initial peptide concentration were compared (Fig. 6 b and d). The binding profile of the HA-2 peptide suggested a specific interaction with HA, while the profile for the HA-3 peptide mimicked that of the Scram peptide, a non-specific interaction. These data were again fit with either model r^a or r^b (Table 2), depending on the qualitative features of the data. Model r^a effectively described the HA-2 peptide data (Fig. 6b) and estimated that HA-2 had bound HA with a lower affinity, higher K_D, and lower non-specific binding, K_N, compared to the full peptide (Table 3). The affinity of HA-2 to HA ($K_D = 54.4\,\mu M \pm 7.6\,\mu M$) was almost 4 times less than that of HA-1 ($K_D = 14.1\,\mu M \pm 3.8\,\mu M$). We also estimated the association rate constants, k_{on}, for HA-1 and HA-2 from the averaged, initial slopes (determined from the initial 2 min of binding) of the respective kinetic profiles for each concentration and found that the HA-1 peptide associated with HA about 2 times faster than the HA-2 peptide (Table 3). As expected, the k_{on} rate constants were generally slower compared to other receptor–ligand interactions [51]. Additionally, we estimated the k_{off} dissociation rate constant via the relation $K_D = k_{off}/k_{on}$ and found the HA-2 peptide dissociated roughly 1.5 time faster than HA-1. Conversely, model r^b matched up with the HA-3 binding data (Fig. 6d) and estimated a K_N very similar to those of peptides HA-1 and Scram (Table 3), suggesting no specific interaction with the HA substrate occurred. It was surprising to us that two fragments of a single peptide behaved so differently, but together exhibit enhanced function.

4. Discussion

SPR has been used by many researchers to quantitatively measure the adsorption kinetics and affinity of small molecules to surfaces [26–28]. To our knowledge, this is the first time SPRi has been used to measure the interaction between a peptide and a biologically relevant mineral such as HA. We successfully developed a HA coated substrate that supported SPR. A PDMS microfluidic device was then coupled to the HA surface allowing us to deliver various concentrations of peptide to six distinct regions on the HA surface. XPS analysis confirmed that our surface was composed primarily of HA and possibly TCP while also having a small fraction of $CaCO_3$. We believe CO_3^{2-} was incorporated into our HA target during the fabrication process which was then translated to our surface during the sputtering process [46,47]. On a macroscopic scale, AFM and SEM imaging showed a uniform HA coating but also microscopic heterogeneities resembling island like features similar to those observed in literature [48–50]. We further determined the sensitivity limit ($\Delta n = 5 \times 10^{-5}$ RIU) of our SPRi system and the conditions under which changes in refractive index (i.e., the mass of adsorbed surface molecules) remained proportional to changes in reflectivity, $\Delta(R_p/R_s) < 0.06$.

Using SPRi and framing the interaction between our peptides and HA in the context of a simple model (Table 2), we quantitatively measured the binding kinetics and affinity of the HA-1 peptide to our HA coated sensor. While the adsorption kinetics showed slight concentration dependence, the steady-state change in reflectivity show a more pronounced concentration dependence that appears to be saturable. Compared to other engineered peptides with high nanomolar binding affinities toward surfaces like Au, Ag, Pt, and TiO_2, HA-1 binds with a low, micromolar affinity ($K_D = 14.1\,\mu M \pm 3.8\,\mu M$) to HA[17, 19, 22, 28, 29]. This interaction is still quite strong considering the unique chemical and structural heterogeneities of HA compared to the relative uniformity of these other materials. In fact, HA-1 bound HA more tightly than an N-terminal 15-amino acid peptide derived from the salivary protein statherin ($K_D \approx 30\,\mu M$) [52].

The HA-1 peptide does not interact with $CaCO_3$ or with amorphous calcium phosphate, providing evidence that both chemical composition and crystalline structure contributes to the interaction with HA [23]. We further probed this observation by challenging our HA surface with fragments of the full length peptide. Not surprisingly, the HA-2 fragment (SVSVGGK-*b*) bound with lower affinity ($K_D = 54.4\,\mu M \pm 7.6\,\mu M$) than the full length HA-1 peptide. This result was surprising since the HA-2 peptide contained no acidic amino acids like most other peptides reported to bind to HA [2,15,16]. Upon further inspection, the only similar feature HA-2 had compared to other HA binding peptides was two closely space serine residues [24,52]. In the case of the statherin peptide, the

Table 3
Parameters characterizing the steady-state binding of HA-specific and non-specific peptides.

Peptide	K_D (μM)	K_N (r μM^{-1})	B_{max} (r)	k_{on} (μM^{-1} min^{-1})	k_{off} (min^{-1})
HA-1	14.1 ± 3.8	$3.0 \times 10^{-5} \pm 5.8 \times 10^{-6}$	0.0156	0.0106 ± 0.0024	0.15 ± 0.136
HA-2	54.4 ± 7.6	$2.6 \times 10^{-5} \pm 4.3 \times 10^{-6}$	0.0156	0.0047 ± 0.00096	0.26 ± 0.126
HA-3	–	$3.9 \times 10^{-5} \pm 2.9 \times 10^{-6}$	–	–	–
Scram	–	$3.3 \times 10^{-5} \pm 6.6 \times 10^{-6}$	–	–	–

r = reflectivity change, $\Delta(R_p/R_s)$. Parameter values are reported as the mean ± the standard deviation. The B_{max}, value was assumed constant for fitting.

serine residues are phosphorylated and the 5 amino acid sequence containing them (DpSpSEE) is structurally immobile when hydrated [53]. It is possible that the HA-2 peptide fragment, acting through the polar serine residues, provides close contact points to Ca^{2+} and aligns with any underlying HA lattice structure.

We next challenged our surface with the HA-3 peptide fragment (VSMKPSPGGGK-*b*) to assess how the trailing sequence of the HA-1 peptide influenced the overall binding affinity. Somewhat strikingly, HA-3 seemed to interact with HA in a non-specific manner, in the context of our r^b model. Fitting the data to the r^a model yielded a good fit, but all the data fell on the linear portion of the binding curve away from the region of highest concentration sensitivity. A lower concentration of HA-3 (2 μM) was tested but again fell in line with the linear trend observed in Fig. 6d (data not shown). Detection of lower concentrations (nanomolar) with the current HA sensor was not possible. Although we cannot definitively say, it seems unlikely that breaking up the full length peptide would generate a peptide with higher affinity than the parent. We speculate that MKPSPG sequence might convey a conformation contribution that enhances the interaction with the HA by stabilizing the interaction of the leading SVSV sequence. In fact, the secondary structure of a peptide is reported to play a role in the interaction with HA. The N-terminal 15-amino acid binding domain of statherin is reported to be α-helical when bound to HA. It has been proposed that the α-helix motif could be used as a scaffolding mechanism to align acidic side-chain residues with HA and promote stabilization of the overall interaction [3,53,54]. While we and others have identified amino acid residues important in mediating the affinity toward HA, further investigation into the precise mechanism of peptide interaction is needed.

5. Conclusions

This study has successfully quantified the binding affinity of a specific HA binding peptide (HA-1) and two HA-1 derived peptide fragments while also providing some clues into the HA binding mechanism. The HA-1 peptide possesses a binding constant that is significantly enhanced over the individual fragments and is sufficient for use as either a probe to monitor biological processes like biomineralization or as a modifier for enhancing the functionalities of implantable, HA coated materials by directing cell function and/or fates through presentation of adhesive sites (RGD) or signaling cues (growth factors or other biomolecules) to cells. We believe it is imperative that the affinity between any probe and its target be assessable to ensure proper application and interpretation of results. The level of material interaction will ultimately impact the effectiveness of each application.

Acknowledgements

The authors gratefully acknowledge support from a National Institute of Standards and Technology (NIST) Innovation in Measurement Science Award in Cellular Biometrology and National Research Council/NIST postdoctoral fellowships to MDR and MCW. The authors would also like to thank Khaled Aamer, Alexander Peterson, Nicole Moore and the NIST Center for Nanoscale Science and Technology for their valuable contributions to this work.

Certain commercial equipment, instruments, or materials are identified in this paper in order to specify the experimental procedure adequately. Such identification is not intended to imply recommendation or endorsement by the National Institute of Standards and Technology, nor is it intended to imply that the materials or equipment identified are necessarily the best available for the purpose. Official contributions of the National Institute of Standards and Technology – Not subject to copyright in the United States.

Appendix

Figure with essential colour discrimination. Figs. 1–6 of this article have parts that may be difficult to interpret in black and white. The full colour images can be found in the online version, at doi:10.1016/j.biomaterials.2010.01.012.

References

[1] Molloy ES, McCarthy GM. Hydroxyapatite deposition disease of the joint. Curr Rheumatol Rep 2003;5(3):215–21.
[2] Fujisawa R, Wada Y, Nodasaka Y, Kuboki Y. Acidic amino acid-rich sequences as binding sites of osteonectin to hydroxyapatite crystals. Biochim Biophys Acta Protein Struc Mol Enz 1996;1292(1):53–60.
[3] Hauschka PV, Carr SA. Calcium-dependent alpha-helical structure in osteocalcin. Biochemistry 1982;21(10):2538–47.
[4] Johnsson M, Levine MJ, Nancollas GH. Hydroxyapatite binding domains in salivary proteins. Crit Rev Oral Biol Med 1993;4(3–4):371–8.
[5] Mann S. Molecular recognition in biomineralization. Nature 1988;332(6160):119–24.
[6] Robey PG, Fedarko NS, Hefferan TE, Bianco P, Vetter UK, Grzesik W, et al. Structure and molecular regulation of bone matrix proteins. J Bone Miner Res 1993;8(Suppl. 2):S483–7.
[7] Gajjeraman S, Narayanan K, Hao JJ, Qin CL, George A. Matrix macromolecules in hard tissues control the nucleation and hierarchical assembly of hydroxyapatite. J Biol Chem 2007;282(2):1193–204.
[8] He G, Dahl T, Veis A, George A. Nucleation of apatite crystals in vitro by self-assembled dentin matrix protein, 1. Nat Mater 2003;2(8):552–8.
[9] Long JR, Dindot JL, Zebroski H, Kiihne S, Clark RH, Campbell AA, et al. A peptide that inhibits hydroxyapatite growth is in an extended conformation on the crystal surface. Proc Natl Acad Sci U S A 1998;95(21):12083–7.
[10] Bills CE, Eisenberg H, Pallante SL. Complexes of organic acids with calcium phosphate: the von kossa stain as a clue to the composition of bone mineral. Johns Hopkins Med J 1974;128(4):194–207.
[11] Gindler EM, King JD. Rapid colorimetric determination of calcium in biologic fluids with methylthymol blue. Am J Clin Pathol 1972;58(4):376–82.
[12] Mcgeerussell SM. Histochemi cal methods for calcium. J Histochem Cytochem 1958;6(1):22–42.
[13] Puchtler H, Meloan SN, Terry MS. On the history and mechanism of alizarin and alizarin red S stains for calcium. J Histochem Cytochem 1969;17(2):110–24.
[14] Fujisawa R, Mizuno M, Nodasaka Y, Kuboki Y. Attachment of osteoblastic cells to hydroxyapatite crystals by a synthetic peptide (Glu(7)-Pro-Arg-Gly-Asp-Thr) containing two functional sequences of bone sialoprotein. Matrix Biol 1997;16(1):21–8.
[15] Itoh D, Yoneda S, Kuroda S, Kondo H, Umezawa A, Ohya K, et al. Enhancement of osteogenesis on hydroxyapatite surface coated with synthetic peptide (EE EEEEEPRGDT) in vitro. J Biomed Mater Res 2002;62(2):292–8.
[16] Shaw WJ, Long JR, Dindot JL, Campbell AA, Stayton PS, Drobny GP. Determination of statherin N-terminal peptide conformation on hydroxya patite crystals. J Am Chem Soc 2000;122(8):1709–16.
[17] Kriplani U, Kay BK. Selecting peptides for use in nanoscale materials using phage-displayed combinatorial peptide libraries. Curr Opin Biotechnol 2005;16(4):470–5.
[18] Smith GP. Filamentous fusion phage: novel expression vectors that display cloned antigens on the virion surface. Science 1985;228(4705):1315–7.
[19] Whaley SR, English DS, Hu EL, Barbara PF, Belcher AM. Selection of peptides with semiconductor binding specificity for directed nanocrystal assembly. Nature 2000;405(6787):665–8.
[20] Sarikaya M, Tamerler C, Jen AK, Schulten K, Baneyx F. Molecular biomimetics: nanotechnology through biology. Nat Mater 2003;2(9):577–85.
[21] Naik RR, Stringer SJ, Agarwal G, Jones SE, Stone MO. Biomimetic synthesis and patterning of silver nanoparticles. Nat Mater 2002;1(3):169–72.
[22] Brown S, Sarikaya M, Johnson E. A genetic analysi s of crystal growth. J Mol Biol 2000;299(3):725–35.
[23] Roy MD, Stanley SK, Amis EJ, Becker ML. Identification of a highly specific hydroxyapatite-binding peptide using ph age display. Adv Mater 2008;20(10):1830–6.
[24] Segvich SJ, Smith HC, Kohn DH. The adsorption of preferential binding peptides to apatite-based materials. Biomaterials 2009;30(7):1287–98.
[25] McDonnell JM. Surface plasmon resonance: towards an understanding of the mechanisms of biological molecular recognition. Curr Opin Chem Biol 2001;5(5):572–7.
[26] So CR, Tamerler C, Sarikaya M. Adsorption, diffusion, and self-assembly of an engineered gold-binding peptide on Au(111) investigated by atomic force microscopy. Angew Chem Int Ed 2009;48(28):5174–7.
[27] Tamerler C, Oren EE, Duman M, Venkatasubramanian E, Sarikaya M. Adsorption kinetics of an engineered gold binding peptide by surface plasmon resonance spectroscopy and a quartz crystal microbalance. Langmuir 2006;22(18):7712–8.
[28] Seker UO, Wilson B, Sahin D, Tamerler C, Sarikaya M. Quantitative affinity of genetically engineered repeating polypeptides to inorganic surfaces. Biomacromolecules 2009;10(2):250–7.

[29] Seker UOS, Wilson B, Dincer S, Kim IW, Oren EE, Evans JS, et al. Adsorption behavior of linear and cyclic genetically engineered platinum binding peptides. Langmuir 2007;23(15):7895–900.
[30] Seah MP, Dench WA. Quantitative electron spectroscopy of surfaces: a standard data base for electron inelastic mean free paths in solids. Surf Interf Anal 1979;1:2–11.
[31] McDonald JC, Duffy DC, Anderson JR, Chiu DT, Wu HK, Schueller OJA, et al. Fabrication of microfluidic systems in poly(dimethylsiloxane). Electrophoresis 2000;21(1):27–40.
[32] Sia SK, Whitesides GM. Microfluidic devices fabricated in poly-(dimethylsiloxane) for biological studies. Electrophoresis 2003;24(21): 3563–76.
[33] Lecaruyer P, Canva M, Rolland J. Metallic film optimization in a surface plasmon resonance biosensor by the extended Rouard method. Appl Opt 2007;46(12):2361–9.
[34] Hanken DG, Jordan CE, Frey BL, Corn RM. Surface plasmon resonance measurements of ultrathin organic films at elect rode surfaces. Electroanal Chem 1998;20:141–225.
[35] Yuan XC, Hong B, Tan YG, Zhang DW, Irawan R, Tjin SC. Sensitivity-stability-optimized surface plasmon resonance sensing with doublemetal layers. J Opt A Pure Appl Opt 2006;8(11):959–63.
[36] Giebel KF, Bechinger C, Herminghaus S, Riedel M, Leiderer P, Weiland U, et al. Imaging of cell/substrate contacts of living cells with surface plasmon resonance microscopy. Biophys J 1999;76(1):509–16.
[37] Nelson SG, Johnston KS, Yee SS. High sensitivity surface plasmon resonance sensor b ased on phase detection. Sens Actuators B 1996;35(1–3):187–91.
[38] Handbook of surface plasmon resonance. RSC Publishing; 2008.
[39] Nancollas GH, Zhang J. Hydroxyapatite and related materials. Boca Raton: CRC Press; 1994.
[40] Kay MI, Young RA, Posner AS. Crystal structure of hydroxyapatite. Nature 1964;204(496):1050–2.
[41] Ozeki K, Aoki H, Fukui Y. Effect of pH on crystallization of sputtered hydroxyapatite film under hydrothermal condition s at low temperature. J Mater Sci 2005;40(11):2837–42.
[42] Lu HB, Campbell CT, Graham DJ, Ratner BD. Surface characterization of hydroxyapatite and related calcium phosphates by XPS and TOF-SIMS. Anal Chem 2000;72(13):2886–94.
[43] Landis WJ, Martin JR. X-ray photoelecton spectroscopy applied to gold-decorated mineral standards of biological interest. J Vac Sci Tech A 1984;2(2):1108–11.
[44] Chusuei CC, Goodman DW, Van Stipdonk MJ, Justes DR, Schweikert EA. Calcium phosphate phase identification using XPS and time-of-flight cluster SIMS. Anal Chem 1999;71(1):149–53.
[45] Tanahashi M, Matsuda T. Surface functional group dependence on apatite formation on self-assembled monolayers in a simulated body fluid. J Biomed Mater Res 1997;34(3):305–15.
[46] Pal'chik NA, Grigor'eva TN, Stolpovskaya VN, Arkhipenko DK, Moroz TN. Effect of synthetic conditions on structural characteristics of hydroxylapatite. Rus J Appl Chem 1997;70(10):1513–6.
[47] Yamashita K, Yagi T, Umegaki T. Bonelike coatings onto ceramics by reacti ve magnetron sputtering. J Am Ceram Soc 1996;79(12):3313–6.
[48] McGall SJ, Davies PB, Neivandt DJ. Development of a biologically relevant calcium phosphate substrate for sum frequency generation vibrational spectroscopy. J Phys Chem A 2005;109(39):8745–54.
[49] Xu SY, Long JD, Sim LN, Diong CH, Ostrikov K. RF plasma sputtering deposition of hydroxyapatite bioceramics: synthesis, performance, and biocompatibility. Plasma Process Polym 2005;2(5):373–90.
[50] Yang YZ, Kim KH, Ong JL. Review on calcium phosphate coatings produced using a sputtering process–an alternative to plasma spraying. Biomaterials 2005;26(3):327–37.
[51] Lauffenburger DA, Linderman JJ. Receptors: models for binding, trafficing, and signalling. Oxford University Press; 1996.
[52] Gilbert M, Shaw WJ, Long JR, Nelson K, Drobny GP, Giachelli CM, et al. Chimeric peptides of statherin and osteopontin that bind hydroxyapatite and mediate cell adhesion. J Biol Chem 2000;275(21):16213–8.
[53] Stayton PS, Drobny GP, Shaw WJ, Long JR, Gilbert M. Molecular recognition at the protein-hydroxyapatite interface. Crit Rev Oral Biol Med 2003;14(5):370–6.
[54] DeOliveira DB, Laursen RA. Control of calcite crystal morphology by a peptide designed to bind to a specific surface. J Am Chem Soc 1997;119(44):10627–31.